Opportunistic Radar in IEEE 802.11ad Networks

Emanuele Grossi ⓘ, *Senior Member, IEEE*, Marco Lops ⓘ, *Senior Member, IEEE*,
Luca Venturino ⓘ, *Senior Member, IEEE*, and Alessio Zappone ⓘ, *Senior Member, IEEE*

Abstract—In this paper, we study the feasibility of an opportunistic radar, which exploits the probing signals transmitted during the sector level sweep of the IEEE 802.11ad beamforming training protocol. Several solutions are presented to detect the presence of prospective obstacles and estimate their position, radial velocity, and backscattered signal amplitude, which differ in the amount of prior information as to the transmitted signal and the channel fluctuation. Also, we derive the Cramér–Rao bound as a benchmark for the proposed estimators: The derivation of these bounds is *per se* relevant, as it generalizes classical results to the case where the echo is not entirely contained in the observation window. Numerical examples are provided to assess performance of the proposed solutions. The results indicate that the close-to-one detection probability is achievable up to 90 m with a probability of false alarm of 1e-4 and Swerling-I target fluctuation; in this region, the target delay is estimated with an accuracy smaller than the symbol interval (corresponding to a range resolution smaller than 10 cm) with probability close to one, while the velocity estimate is generally quite poor as a consequence of the very short duration of the probing signal.

Index Terms—Opportunistic radar, Cramér-Rao bound, generalized likelihood ratio test, mmWaves, 60 GHz, IEEE 802.11ad.

I. Introduction

A MAJOR trend in terrestrial wireless networks, and in particular in fifth-generation (5G) systems [1]–[3], is to scale up the carrier frequency towards millimeter waves (mmWave's) [4], [5], so as to support bandwidths in the order of hundreds of MHz; carrier frequencies as high as 28 GHz and 60 GHz have been proposed in [6], [7]. This is steering the academic and industrial interest back to the investigation of the physical propagation effects in the EHF bandwidth, as well as to the issue of channel modeling for mmWaves [8]–[10], traditionally employed in radio-astronomy from high-altitude sites

and satellite-based remote sensing. When used for terrestrial applications, mmWaves suffer from heavy atmospheric attenuation, resonance in the O_2 molecule, absorption by rain, and almost complete shadowing by obstacles. As a consequence, they require the presence of a line-of-sight path between the transmitter and the receiver and the use of high-gain directional antennas [11]–[14].

Directional links at mmWaves are established by resorting to sophisticated beamforming protocols which sense the surrounding scene to determine the best transmit/receive sectors: this is naturally conducive to investigating *integrated multi-functional* systems, wherein some radar operations are accomplished by exploiting mmWave communication signals [15]. The idea of communication and surveillance systems sharing the same bandwidth is not new, as demonstrated by the large body of studies devoted to the design of co-existing architectures [16], [17]. The basic philosophy put forward in [18]–[22] is to mitigate the mutual interference produced by two independent, concurrent systems, which compete for common resources. More generally, all monitoring-oriented applications can benefit from the radar and communication integration. Indeed, there is a growing interest towards performing tasks like intrusion detection, restricted area surveillance, patient monitoring, child and elder home-care without using dedicated devices [23]–[27].

In this paper, we explore the possibility of implementing key radar surveillance functions, such as the detection of prospective obstacles and their localization in the range-Doppler domain, by exploiting the echoes generated during the beamforming training protocol of the IEEE 802.11ad standard operating at 60 GHz [28]–[31]. In this context, the proposed radar is defined *opportunistic*, since it only consists of a receiver, co-located with the communication transceiver, and a dedicated software chain aimed at processing the received signal; the receiver can avail itself of some side information, such as the timing, the azimuth and even the transmitted data, but does not have otherwise any impact on the *primary* communication system, nor does it generate any co-existence problem. Such an opportunistic architecture has nothing to do with *passive radars*, which have little or no information as to the received signals and in fact need multiple sources for target localization [32]; instead, our approach is similar in spirit to the one followed in [33], where the authors study the possibility of using the IEEE 802.11p standard to implement an automotive OFDM-radar at 5.9 GHz, and in [34], where the preamble detector from [35] is used to estimate the position and the velocity of another node (i.e., a car) in an IEEE 802.11ad network after having established a directional link.

Starting form the preliminary results presented by the authors in [36], [37], this study aims at verifying the feasibility of such an opportunistic architecture and at investigating the achievable performance in terms of obstacle detection *and* localization in the range-velocity plane. Indeed, this information is helpful not only for collision avoidance, traffic management, or intrusion detection, but also to facilitate some operations of the communication module, such as channel estimation and beam alignment, if the detected object is another network device. After presenting the model for the signal scattered towards the radar receiver during the sector level sweep (SLS) phase of the beamforming training protocol, we make the following major contributions.

- We introduce novel detection structures and discuss their implementation complexity. The proposed schemes are derived by solving a generalized likelihood ratio test (GLRT) under different design assumptions concerning the transmitted signal and the channel fluctuation. As a by product, we also provide the corresponding maximum likelihood (ML) estimators of the range (delay), velocity (Doppler), and signal amplitude of a detected object.

- We provide the Cramér-Rao bound (CRB) as a benchmark for the proposed estimators: the derivation is novel and *per-se* relevant, as it generalizes classical results to the case where the echo is not entirely contained in the observation window. This analysis reveals that the achievable accuracy in the velocity estimation is limited by the very short duration of the probing signal, and, hence, may not be adequate for some commercial applications; instead, the achievable accuracy in the range estimation may be well-below the cm-level, as a consequence of the large bandwidth.

- We provide a numerical study to assess the detection and estimation performance of the proposed solutions. The analysis shows that, for a probability of false alarm of 1e-4 and Swerling-I target fluctuation, the proposed receive chain outperforms the preamble-based detector adopted in [34], granting a close-to-one probability of detection and a close-to-one probability of estimating the target delay with an accuracy smaller than the symbol interval (corresponding to a range resolution smaller than 10 cm) up to 90 meters.

The remainder of this work is organized as follows. Section II contains the system description. Section III contains the derivation of the GLRT under four different design assumptions. Section IV discusses the implementation of the proposed solutions. Section V contains the derivation of the CRB for the estimators of range, velocity, and signal amplitude. Section VI is devoted to the numerical analysis. Finally, concluding remarks are provided in Section VII, while the Appendix contains some mathematical derivations.

II. SYSTEM DESCRIPTION

The IEEE 802.11ad standard defines a communication scheme that takes advantage of beamforming to cope with the severe attenuation in the 60 GHz band [28]–[31], [38]. Planar antenna arrays are used in mmWave communications to obtain a
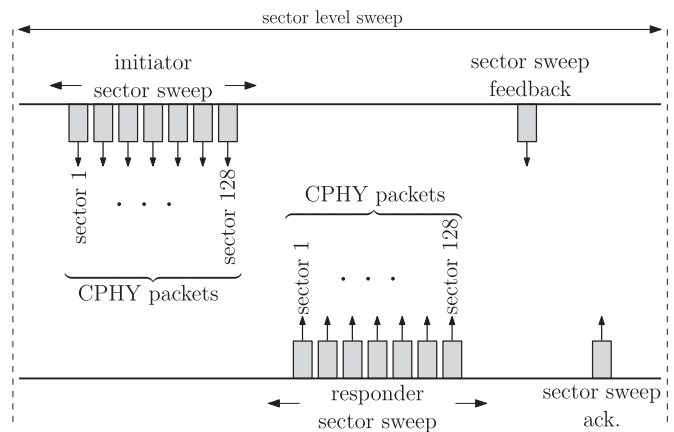

Fig. 1. Description of the sector level sweep in the IEEE 802.11ad standard.

highly-directional beam in both azimuth and elevation, which results into reduced inter-user (spatial) interference and increased capacity [39]. With quasi-optical propagation behavior, low reflectivity, and high attenuation, transmit and receive beams need to be aligned for data communication; for this reason, the standard supports beam steering towards up to 128 distinct sectors. In order to establish a directional link, two neighboring nodes execute a beamforming training protocol consisting of a SLS and an optional beam refinement (BR). During the SLS phase, a coarse-grain antenna sector configuration is determined; then, this information is used in the BR phase to fine-tune the selected sector. We focus on the SLS phase, which involves four steps, namely, an initiator sector sweep (ISS), a responder sector sweep (RSS), a sector sweep feedback (SSF), and a sector sweep acknowledgement (SSA), as described below (see also Fig. 1).

1) *ISS:* One node, called initiator, starts the procedure by performing a sequence of directional transmissions towards the available sectors. The other node, called responder, receives in quasi omni-directional (QO) mode and determines the transmit sector of the initiator with the largest signal-to-noise ratio (SNR).

2) *RSS:* The roles of initiator and responder are then reversed. The responder starts a sector sweep, while the initiator receives in QO mode and determines the transmit sector of the responder with the largest SNR. During this step, each transmission also carries the information as to the best transmit sector for the initiator.

3) *SSF:* The initiator sends a feedback frame to the responder with its best transmit sector.

4) *SSA:* The procedure ends when the responder acknowledges the reception of the feedback frame.

Each transmission in the SLS consists of a control physical (CPHY) packet that contains a preamble, a header, and a payload.[1] The preamble contains 7752 symbols and is formed by the concatenation of a pair of Golay complementary sequences of length 128, as shown in Fig. 2. The digital modulator employs

---

[1]An optional beamforming training field can be appended to the CPHY packet. For the sake of simplicity and without loss of generality, we do not use this optional field.
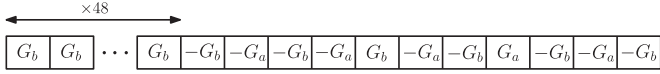
Fig. 2. Preamble of CPHY packet in the IEEE 802.11ad standard. G_a and G_b are Golay complementary sequences of length 128.
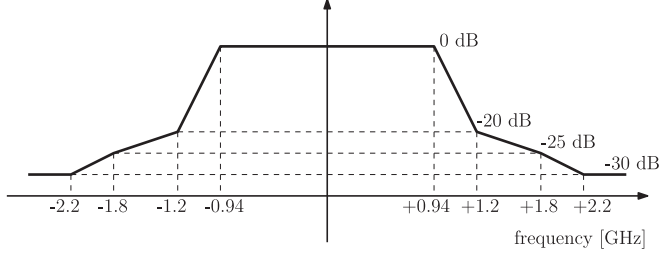

Fig. 3. Baseband spectrum mask of the IEEE 802.11ad standard.

a $\frac{\pi}{2}$-binary phase shift keying (BPSK) scheme which outputs the following baseband waveform:

$$s(t) = \sum_{k=0}^{K-1} b(k)\psi(t - kT), \quad t \in [0, T_s) \tag{1}$$

where K is the number of symbols in the CPHY packet, $\boldsymbol{b} = \big(b(1), \ldots, b(K)\big) \in \mathcal{B}$ is the sequence of transmitted symbols, $\mathcal{B} \subseteq \{-1, 1, -\mathrm{i}, \mathrm{i}\}^K$ is the set of feasible sequences, $\psi(t)$ is a pulse with support in $[0, T_\psi)$, T is the symbol interval, and $T_s = (N - 1)T + T_\psi$ is the packet duration. The standard specifies the symbol rate, namely, $1/T = 1760$ MHz, and the spectrum mask reported in Fig. 3, but not the baseband pulse $\psi(t)$. When the transmission of $s(t)$ is concluded, the antenna beam is steered toward the next sector, and a new CPHY packet is transmitted; the procedure continues until the whole area is inspected.

A. Opportunistic Radar

The sequence of directional transmissions performed during the ISS or RSS phase can be used for sensing the surrounding environment: specifically, if the transmitted signal hits an object, then its echo can be detected. Exploring the feasibility of such an opportunistic radar system appears of great interest, as it could add handy features to devices complying with the 802.11ad standard with limited additional costs.

The problem appears challenging, as the scanning protocol has been designed for a different application. Indeed, if the distance of a prospective object is smaller than $cT_s/2$, with c being the speed of light, the reception of its echo starts while the transmission of the CPHY packet is still on going. This requires that the node be equipped with separate transmit and receive chains which are capable of full-duplex operation on the same frequency band. This feature can be foreseen thanks to the use of efficient circulators and self-interference cancellation mechanisms [40]–[43]: indeed, these technologies have already been proved to be effective in IEEE 802.11 networks [44] and at mmWaves [45]. Also, notice that the transmit antenna is steered towards the next angular sector after completing the

transmission of each CPHY packet; since the receive antenna beam must be aligned with the transmit one for signal detection, only a portion of the echo generated by a prospective object can be observed in each probed direction. Finally, the transmit waveform in (1) is not optimized for radar applications, and its delay-Doppler ambiguity function [46] depends on the control and payload bits to be transmitted.

At the design stage, we make the following simplifying assumptions, which allow deriving a tractable mathematical model, while still capturing the essence of the problem.

- Whenever multiple physical objects are present in the probed sector, we assume that the closest one is sufficiently large with respect to the antenna beamwidth and carrier wavelength to block the signal propagation: this is not a stringent requirement for short range applications, as the standard adopts a highly-directional transmit beam and operates with a carrier wavelength of $\lambda = 5$ mm.
- The object causing the echo can be any physical obstacle present in the environment, such as another network node, a wall, a person, a tree, a car, etc. We do not discriminate among scatterers of different nature, but any reverberation from the environment, including surface clutter,[2] is deemed as a signal to be detected: the goal here is to obtain a map of the free space surrounding the transmit node, which may be helpful in both automotive and intrusion-detection applications.
- We assume line-of-sight signal propagation. This is motivated by the fact that the strength of a non-direct ray (if present) is usually much weaker than the strength of the direct one: indeed, a non-direct path is longer, involve at least one additional reflection, and is typically not aligned with the receive beam.
- We neglect the reflections from objects in adjacent sectors, as the two-way beam-pattern of mmWaves antennas typically has very small sidelobes.

As a consequence of these assumptions, at most one echo can be present in each probed sector and, hence, we must distinguish between its presence (hypothesis H_1) and its absence (hypothesis H_0); specifically, we are faced with the following hypothesis testing problem:

$$r(t) = \begin{cases} A\mathrm{e}^{2\pi\mathrm{i}\nu t}s(t - \tau) + w(t), & t \in [0, T_r), \text{ under } H_1 \\ w(t), & t \in [0, T_r), \text{ under } H_0 \end{cases} \tag{2}$$

where

- $T_r \leq T_s + T_\ell$ is the length of the observation window, where T_ℓ is the (possible) latency time between transmissions in successive angular sectors;
- $r(t) \in \mathbb{C}$ is the baseband received signal;
- $A \in \mathbb{C}$, $\nu \in \mathbb{R}$ and $\tau \in [0, T_r)$ are the amplitude, Doppler shift, and delay of the received echo; notice that A is a function of the two-way antenna gain, the two-way channel response, and the radar cross-section (RCS) of the obstacle causing the reflection;

---

[2]We do not consider here weather clutter.

- finally, $w(t) \in \mathbb{C}$ is a circularly-symmetric white Gaussian process with power spectral density equal to σ^2, accounting for the thermal noise and, possibly, the residual interference after self-interference cancellation.

III. DETECTOR DESIGN

H_1 is a composite hypothesis, as a number of parameters related to the received echo may be unknown. Let $\boldsymbol{\theta} \in \Theta$ be the vector of unknowns, with Θ denoting the parameter space; also, let $\Lambda_{\boldsymbol{\theta}}$ be the likelihood ratio (LR) between H_1 and H_0 for a fixed $\boldsymbol{\theta} \in \Theta$. We solve the testing problem in (2) by resorting to a GLRT, i.e.,

$$\max_{\boldsymbol{\theta} \in \Theta} \ln \Lambda_{\boldsymbol{\theta}} \underset{H_0}{\overset{H_1}{\gtrless}} \gamma \qquad (3)$$

where γ is the detection threshold. Clearly, $\boldsymbol{\theta}$ includes the delay τ and the Doppler shift ν, as the position and velocity of a prospective obstacle are typically unknown; we assume here that $\tau \in \mathcal{T} = [0, \tau_{\max}]$ and $\nu \in \mathcal{V} = [-\nu_{\max}, \nu_{\max}]$, where $\tau_{\max} \in [0, T_r]$ and $\nu_{\max} \geq 0$ are the maximum inspected delay and Doppler shift, respectively. Also, the sequence of transmitted symbols can be assumed either known or unknown at the design stage; indeed, even if transmitter and receiver are co-located, exploiting the knowledge of $\boldsymbol{b}$ would require a memory buffer to temporarily store the transmitted symbols, which may be expensive for large values of K. Finally, we may treat A either as an unknown parameter or as a realization of a random variable with a known statistical description.

In the remainder of this section we derive the GLRT in (3) in the following cases:

1) $\boldsymbol{\theta} = (\tau, \nu, A)$, with $\Theta = \mathcal{T} \times \mathcal{V} \times \mathbb{C}$;
2) $\boldsymbol{\theta} = (\tau, \nu)$, with $\Theta = \mathcal{T} \times \mathcal{V}$ and Swerling I or V signal fluctuation;
3) $\boldsymbol{\theta} = (\tau, \nu, A, \boldsymbol{b})$, with $\Theta = \mathcal{T} \times \mathcal{V} \times \mathbb{C} \times \mathcal{B}$;
4) $\boldsymbol{\theta} = (\tau, \nu, \boldsymbol{b})$, with $\Theta = \mathcal{T} \times \mathcal{V} \times \mathcal{B}$ and Swerling I or V signal fluctuation.

A. GLRT: Case 1

In this case, the log-LR (LLR) is [47]

$$\ln \Lambda_{\boldsymbol{\theta}} = 2\Re \left\{ \frac{A^*}{\sigma^2} \int_0^{T_r} r(t) e^{-2\pi i \nu t} s^*(t - \tau) dt \right\}$$
$$- \frac{|A|^2}{\sigma^2} \int_0^{T_r} |s(t - \tau)|^2 dt \qquad (4)$$

where $(\cdot)^*$ denotes conjugate. Upon defining

$$r_{\tau,\nu}(k) = \int_0^{T_r} r(t) e^{-2\pi i \nu t} \psi^*(t - kT - \tau) dt \qquad (5)$$

$$\mathcal{E}_\tau = \int_0^{T_r} |s(t - \tau)|^2 dt \qquad (6)$$

$$d_\tau = \min \left\{ \left\lceil \frac{T_r - \tau}{T} \right\rceil, K \right\} \qquad (7)$$

where $r_{\tau,\nu}(k)$ is the projection of the received signal along $e^{2\pi i \nu t} \psi(t - kT - \tau)$, $\mathcal{E}_\tau$ is the energy of $s(t - \tau)$ contained in

the observation window, and d_τ is the number of $\frac{\pi}{2}$-BPSK symbols falling in the observation window, Eq. (4) can equivalently be rewritten as

$$\ln \Lambda_{\boldsymbol{\theta}} = 2\Re \left\{ \frac{A^*}{\sigma^2} \sum_{k=0}^{d_\tau - 1} r_{\tau,\nu}(k) b^*(k) \right\} - \frac{|A|^2 \mathcal{E}_\tau}{\sigma^2}. \qquad (8)$$

For fixed τ and ν, the LLR is maximized over A when

$$A = \frac{1}{\mathcal{E}_\tau} \sum_{k=0}^{d_\tau - 1} r_{\tau,\nu}(k) b^*(k) \qquad (9)$$

whereby the GLRT in (3) becomes

$$\max_{(\tau,\nu) \in \mathcal{T} \times \mathcal{V}} \frac{1}{\sigma^2 \mathcal{E}_\tau} \left| \sum_{k=0}^{d_\tau - 1} r_{\tau,\nu}(k) b^*(k) \right|^2 \underset{H_0}{\overset{H_1}{\gtrless}} \gamma. \qquad (10)$$

The maximization over the variables (τ, ν) can be approximated by a grid search [46], [48]. As common in radar applications, we may use a uniformly-spaced grid, namely, $\mathcal{G} = \{(m\Delta_\tau, n\Delta_\nu), \ m = 1, \ldots, M, \ n = -N, \ldots, N\}$, where Δ_τ and Δ_ν are the sampling interval in the delay and Doppler domain, respectively, $M = \lfloor \tau_{\max}/\Delta_\tau \rfloor$, and $N = \lfloor \nu_{\max}/\Delta_\nu \rfloor$; in this case, the GLRT becomes

$$\max_{(\tau,\nu) \in \mathcal{G}} \frac{1}{\sigma^2 \mathcal{E}_\tau} \left| \sum_{k=0}^{d_\tau - 1} r_{\tau,\nu}(k) b^*(k) \right|^2 \underset{H_0}{\overset{H_1}{\gtrless}} \gamma. \qquad (11)$$

B. GLRT: Case 2

We model here the received signal amplitude as

$$A = \alpha e^{i\phi} h_\tau \qquad (12)$$

where $\alpha e^{i\phi}$ is a complex parameter accounting for the signal fluctuation, with $\alpha > 0$ and $\phi \in [0, 2\pi)$, and $h_\tau > 0$ is a delay-dependent term accounting for the two-way antenna gain and path-loss, and the RCS of the obstacle causing the reflection. At the design stage, we assume that ϕ is uniformly distributed, while α is either Rayleigh distributed with $E[|\alpha|^2] = 1$ (Swerling I) or equal to one (Swerling V). Also, we assume that h_τ is known; indeed, the path loss can be either estimated by on-field measurements or predicted via numerical models, while the RCS can either be known in the application at hand or set at a nominal value, usually the one corresponding to the minimum detectable signal at the maximum inspected range.

For Swerling I, the LR conditioned on α and ϕ is

$$\Lambda_{\boldsymbol{\theta}}(\alpha, \phi) = \exp \left\{ 2\Re \left\{ \frac{\alpha e^{-i\phi} h_\tau}{\sigma^2} \sum_{k=0}^{d_\tau - 1} r_{\tau,\nu}(k) b^*(k) \right\} \right.$$
$$\left. - \frac{\alpha^2 h_\tau^2 \mathcal{E}_\tau}{\sigma^2} \right\} \qquad (13)$$

so that

$$\Lambda_{\boldsymbol{\theta}} = \mathrm{E}\left[\mathrm{E}\left[\Lambda_{\boldsymbol{\theta}}(\alpha, \phi)\right] \mid \alpha\right]$$

$$= \mathrm{E}\left[I_0\left(\frac{2\alpha h_\tau}{\sigma^2}\left|\sum_{k=0}^{d_\tau-1} r_{\tau,\nu}(k)b^*(k)\right|\right)\exp\left\{-\frac{\alpha^2 h_\tau^2 \mathcal{E}_\tau}{\sigma^2}\right\}\right]$$

$$= \exp\left\{\frac{h_\tau^2}{\sigma^2(\sigma^2 + h_\tau^2 \mathcal{E}_\tau)}\left|\sum_{k=0}^{d_\tau-1} r_{\tau,\nu}(k)b^*(k)\right|^2\right\}$$

$$\times \left(1 + \frac{h_\tau^2 \mathcal{E}_\tau}{\sigma^2}\right)^{-1} \tag{14}$$

where I_0 is the modified Bessel function of the first kind and order zero. Maximizing the LLR over the values of (τ, ν) in the grid $\mathcal{G}$ leads to the following GLRT

$$\max_{(\tau,\nu)\in\mathcal{G}}\left\{\frac{h_\tau^2}{\sigma^2(\sigma^2 + h_\tau^2 \mathcal{E}_\tau)}\left|\sum_{k=0}^{d_\tau-1} r_{\tau,\nu}(k)b^*(k)\right|^2 \right.$$
$$\left. - \ln\left(1 + \frac{h_\tau^2 \mathcal{E}_\tau}{\sigma^2}\right)\right\} \underset{H_0}{\overset{H_1}{\gtrless}} \gamma. \tag{15}$$

For Swerling V, instead, the LR is

$$\Lambda_{\boldsymbol{\theta}} = \mathrm{E}\left[\Lambda_{\boldsymbol{\theta}}(1, \phi)\right]$$

$$= I_0\left(\frac{2h_\tau}{\sigma^2}\left|\sum_{k=0}^{d_\tau-1} r_{\tau,\nu}(k)b^*(k)\right|\right)\exp\left\{-\frac{h_\tau^2 \mathcal{E}_\tau}{\sigma^2}\right\} \tag{16}$$

which gives the following GLRT

$$\max_{(\tau,\nu)\in\mathcal{G}}\left\{\ln I_0\left(\frac{2h_\tau}{\sigma^2}\left|\sum_{k=0}^{d_\tau-1} r_{\tau,\nu}(k)b^*(k)\right|\right) - \frac{h_\tau^2 \mathcal{E}_\tau}{\sigma^2}\right\} \underset{H_0}{\overset{H_1}{\gtrless}} \gamma. \tag{17}$$

C. GLRT: Case 3

Paralleling the derivation in Section III-A, we obtain the following GLRT

$$\max_{(\tau,\nu,\boldsymbol{b})\in\mathcal{G}\times\mathcal{B}} \frac{1}{\sigma^2 \mathcal{E}_\tau}\left|\sum_{k=0}^{d_\tau-1} r_{\tau,\nu}(k)b^*(k)\right|^2 \underset{H_0}{\overset{H_1}{\gtrless}} \gamma. \tag{18}$$

The maximization over $\boldsymbol{b}$ is unfeasible in practice, as the cardinality of the discrete set $\mathcal{B}$ is exponential with the packet length. To overcome this issue, we relax the search set to $\overline{\mathcal{B}} = \{\boldsymbol{x} \in \mathbb{C}^K : |x_k| = 1\}$. In this latter case, exploiting the triangle inequality, we have that

$$\max_{\boldsymbol{b}\in\overline{\mathcal{B}}}\left|\sum_{k=0}^{d_\tau-1} r_{\tau,\nu}(k)b^*(k)\right| = \sum_{k=0}^{d_\tau-1} |r_{\tau,\nu}(k)| \tag{19}$$

achieved for

$$b(k) = \frac{r_{\tau,\nu}(k)}{|r_{\tau,\nu}(k)|}, \quad k = 0, \ldots, d_\tau \tag{20}$$

and the GLRT in (18) becomes

$$\max_{(\tau,\nu)\in\mathcal{G}} \frac{1}{\sigma^2 \mathcal{E}_\tau}\left(\sum_{k=0}^{d_\tau-1} |r_{\tau,\nu}(k)|\right)^2 \underset{H_0}{\overset{H_1}{\gtrless}} \gamma. \tag{21}$$

D. GLRT: Case 4

As in Section III-C, we approximate the maximization over $\boldsymbol{b}$ by relaxing the search set to $\overline{\mathcal{B}}$. Hence, paralleling the derivations in Section III-B, the GLRT under Swerling I and V are easily shown to be

$$\max_{(\tau,\nu)\in\mathcal{G}}\left\{\frac{h_\tau^2}{\sigma^2(\sigma^2 + h_\tau^2 \mathcal{E}_\tau)}\left(\sum_{k=0}^{d_\tau-1} |r_{\tau,\nu}(k)|\right)^2 \right.$$
$$\left. - \ln\left(1 + \frac{h_\tau^2 \mathcal{E}_\tau}{\sigma^2}\right)\right\} \underset{H_0}{\overset{H_1}{\gtrless}} \gamma \tag{22}$$

and

$$\max_{(\tau,\nu)\in\mathcal{G}}\left\{\ln I_0\left(\frac{2h_\tau}{\sigma^2}\sum_{k=0}^{d_\tau-1} |r_{\tau,\nu}(k)|\right) - \frac{h_\tau^2 \mathcal{E}_\tau}{\sigma^2}\right\} \underset{H_0}{\overset{H_1}{\gtrless}} \gamma \tag{23}$$

respectively.

IV. GLRT IMPLEMENTATION

The solutions proposed in Section III depend on

$$C_{\tau,\nu} = \sum_{k=0}^{d_\tau-1} r_{\tau,\nu}(k)b^*(k) \tag{24}$$

if $\boldsymbol{b}$ is known, or

$$F_{\tau,\nu} = \sum_{k=0}^{d_\tau-1} |r_{\tau,\nu}(k)| \tag{25}$$

otherwise. The statistics $C_{\tau,\nu}$ and $F_{\tau,\nu}$ can be interpreted as the output of a coherent and an incoherent signal integrator, respectively, when a prospective object is assumed to have delay τ and Doppler shift ν. They can be computed by first sending the signal $r(t)e^{-2\pi i\nu t}$ to a filter matched to the transmit pulse $\psi(t)$, then sampling its output at the epochs $\{\tau + kT\}_{k=0}^{d_\tau-1}$, and finally elaborating the samples $\{r_{\tau,\nu}(k)\}_{k=0}^{d_\tau-1}$, as shown in Fig. 4. The computation of $\{C_{m\Delta_\tau,\nu}\}_{m=1}^M$ and $\{F_{m\Delta_\tau,\nu}\}_{m=1}^M$ greatly simplifies if $\Delta_\tau = T/Q$, where Q is a strictly-positive integer. Indeed, letting

$$y_\nu(\ell) = \int_0^{T_r} r(t)e^{-2\pi i\nu t}\psi^*(t - \ell T/Q)dt \tag{26}$$

be the sample of the output of the matched filter taken at epoch $\ell T/Q$, for $\ell = 0, \ldots, \lceil T_r Q/T \rceil - 1$, we have

$$C_{mT/Q,\nu} = \sum_{k=0}^{d_{mT/Q}-1} y_\nu(kQ + m)b^*(k) \tag{27a}$$

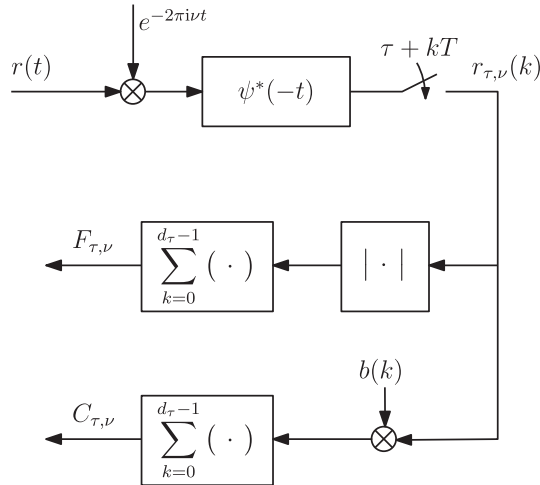$$F_{mT/Q,\nu} = \sum_{k=0}^{d_{mT/Q}-1} |y_\nu(kQ + m)| \tag{27b}$$

Fig. 4. Computation of the test statistics $C_{\tau,\nu}$ and $F_{\tau,\nu}$.

which, for $Q = 1$, simplify to

$$C_{mT/Q,\nu} = y_\nu(m) * b^*(-m) \tag{28a}$$

$$F_{mT/Q,\nu} = |y_\nu(m)| * R_K(-m) \tag{28b}$$

where $*$ denotes convolution and $R_K(m)$ is a sequence whose samples are one if $m \in \{0, \ldots, K-1\}$ and zero otherwise; notice that in (28) we are implicitly assuming that the samples of the sequence $\{b(m)\}_{m=-\infty}^{+\infty}$ are zero if $m \notin \{0, \ldots, K-1\}$ and that the samples of the sequence $\{y_\nu(m)\}_{m=-\infty}^{+\infty}$ are zero if $m \notin \{0, \ldots, \lceil T_r/T \rceil - 1\}$.

A. Computational Complexity

The implementation of the GLRTs in (11), (15), (17), (21), (22), and (23) requires

- acquiring the $\lceil T_r Q/T \rceil$ samples in (26) for the $(2N+1)$ inspected values of ν;
- computing either one of the statistics in (27) for all delays and Doppler shifts, which entails $(2N+1)\sum_{m=1}^{M}(d_{mT/Q} - 1)$ additions and $(2N+1)\sum_{m=1}^{M} d_{mT/Q}$ multiplications/moduli;
- computing the maximum among $(2N+1)M$ elements;

whereby the complexity scales linearly with the length of the observation interval and with the cardinality of the grid. Given the computational resources, T_r must be chosen so that the test is completed before moving to the next angular sector.

Notice also that the maximization over the variable ν in (21), (22), and (23) can be avoided in practice: indeed, due the large transmit bandwidth, we have $\nu_{\max} T_\psi \ll 1$ and,[3] therefore,

$$|r_{\tau,\nu}(k)| = \left| \int_{kT+\tau}^{\min\{T_r, kT+\tau+T_\psi\}} r(t) e^{-2\pi i\nu t} \psi^*(t - kT - \tau) dt \right|$$

$$\approx |r_{\tau,0}(k)|. \tag{29}$$

---

[3]Notice that $1/T_\psi$ is in the order of the symbol rate; therefore a maximum speed of 200 km/h corresponds to $\nu_{\max} \approx 22$ kHz, and $\nu_{\max} T_\psi$ is in the order of 10^{-5}.

B. Parameter Estimation

The tests in (11), (15), (17), (21), (22), and (23) provide, as a by-product, an estimate of the distance, say $\hat{r}$, and of the radial velocity, say $\hat{v}$, of a detected object, i.e.,

$$\hat{r} = \frac{c}{2}\hat{\tau} \tag{30a}$$

$$\hat{v} = \frac{\lambda}{2}\hat{\nu} \tag{30b}$$

where $\hat{\tau}$ and $\hat{\nu}$ are the maximizers of the corresponding objective function. Clearly, the estimate of the radial velocity obtained from the solutions in (21), (22), and (23) is unreliable, as a consequence of (29).

The GLRT (11) also provides, as a by-product, an estimate of the signal amplitude A, namely,

$$\widehat{A} = \frac{1}{\mathcal{E}_{\hat{\tau}}} \sum_{k=0}^{d_{\hat{\tau}}} r_{\hat{\tau},\hat{\nu}}(k) b^*(k) \tag{31}$$

while (21) provides an estimate of $\rho = |A|$, namely,

$$\hat{\rho} = \frac{1}{\mathcal{E}_{\hat{\tau}}} \sum_{k=0}^{d_{\hat{\tau}}} |r_{\hat{\tau},\hat{\nu}}(k)|. \tag{32}$$

Interestingly, this side information could also be exploited by the communication module for channel estimation.

V. CRAMÉR-RAO BOUND

We derive here the CRB for the case treated in Section III-A. Since A is complex, we describe it by its modulus, say ρ, and phase, say φ, and consider the (equivalent) real parameter vector $\boldsymbol{\theta} = (\tau, \nu, \rho, \varphi)$, with parameter space $\Theta = \mathcal{T} \times \mathcal{V} \times (0, \infty) \times \mathbb{R}$. It is desired to estimate $\boldsymbol{x} = (r, v, \rho, \varphi)^T = \boldsymbol{g}(\boldsymbol{\theta})$, where $\boldsymbol{g}(\boldsymbol{\theta}) = (c\theta_1/2, \lambda\theta_2/2, \theta_3, \theta_4)^T$. Let $\hat{\boldsymbol{x}} = (\hat{r}, \hat{v}, \hat{\rho}, \hat{\varphi})^T$ be an unbiased estimator of $\boldsymbol{x}$, $\boldsymbol{C}_{\hat{\boldsymbol{x}}}$ the covariance matrix of $\hat{\boldsymbol{x}}$, $\boldsymbol{J}$ the Fisher information matrix, and

$$\boldsymbol{D} = \begin{pmatrix} \frac{c}{2} & 0 & 0 & 0 \\ 0 & \frac{\lambda}{2} & 0 & 0 \\ 0 & 0 & 1 & 0 \\ 0 & 0 & 0 & 1 \end{pmatrix} \tag{33}$$

the Jacobian of $\boldsymbol{g}(\boldsymbol{\theta})$. Then, the *Information inequality theorem* (also known as CRB) [46], [49], [50] states that the matrix $\boldsymbol{C}_{\hat{\boldsymbol{x}}} - \boldsymbol{D}\boldsymbol{J}^{-1}\boldsymbol{D}^T$ is positive semidefinite. In particular, the variances of the individual errors are bounded by the diagonal elements of $\boldsymbol{D}\boldsymbol{J}^{-1}\boldsymbol{D}^T$, i.e.,

$$\mathrm{E}\left[(\hat{r} - r)^2\right] \geq \left(\frac{c}{2}\right)^2 (\boldsymbol{J}^{-1})_{11} \tag{34a}$$

$$\mathrm{E}\left[(\hat{v} - v)^2\right] \geq \left(\frac{\lambda}{2}\right)^2 (\boldsymbol{J}^{-1})_{22} \tag{34b}$$

$$\mathrm{E}\left[(\hat{\rho} - \rho)^2\right] \geq (\boldsymbol{J}^{-1})_{33} \tag{34c}$$

$$\mathrm{E}\left[(\hat{\varphi} - \varphi)^2\right] \geq (\boldsymbol{J}^{-1})_{44} \tag{34d}$$

Upon defining $s_1 = \frac{ds}{dt}$ and

$$\overline{f_\tau^2} = \frac{1}{(2\pi)^2 \mathcal{E}_\tau} \int_0^{T_r} |s_1(t-\tau)|^2 dt \tag{35a}$$

$$\overline{f}_\tau = \frac{i}{2\pi \mathcal{E}_\tau} \int_0^{T_r} s(t-\tau) s_1^*(t-\tau) dt \tag{35b}$$

$$\beta_\tau = \sqrt{\overline{f_\tau^2} - |\overline{f}_\tau|^2} \tag{35c}$$

$$\overline{t_\tau^2} = \frac{1}{\mathcal{E}_\tau} \int_0^{T_r} t^2 |s(t-\tau)|^2 dt \tag{35d}$$

$$\overline{t}_\tau = \frac{1}{\mathcal{E}_\tau} \int_0^{T_r} t |s(t-\tau)|^2 dt \tag{35e}$$

$$\delta_\tau = \sqrt{\overline{t_\tau^2} - \overline{t}_\tau^2} \tag{35f}$$

$$\overline{ft}_\tau = \frac{1}{2\pi \mathcal{E}_\tau} \Im \left\{ \int_0^{T_r} t s(t-\tau) s_1^*(t-\tau) dt \right\} \tag{35g}$$

$$\xi_\tau = \overline{ft}_\tau + \Re\{\overline{f}_\tau\}\overline{t}_\tau \tag{35h}$$

we have that (34) becomes

$$\mathrm{E}\left[(\hat{r}-r)^2\right] \geq \frac{\left(\frac{c}{2}\right)^2}{\frac{2\mathcal{E}_\tau}{\sigma^2}(2\pi\rho)^2} \frac{1}{\beta_\tau^2 - \frac{\xi_\tau^2}{\delta_\tau^2}} \tag{36a}$$

$$\mathrm{E}\left[(\hat{v}-v)^2\right] \geq \frac{\left(\frac{\lambda}{2}\right)^2}{\frac{2\mathcal{E}_\tau}{\sigma^2}(2\pi\rho)^2} \frac{1}{\delta_\tau^2 - \frac{\xi_\tau^2}{\beta_\tau^2}} \tag{36b}$$

$$\mathrm{E}\left[(\hat{\rho}-\rho)^2\right] \geq \frac{1}{\frac{2\mathcal{E}_\tau}{\sigma^2}} \left(1 + \frac{\Im^2\{\overline{f}_\tau\}}{\beta_\tau^2 - \frac{\xi_\tau^2}{\delta_\tau^2}}\right) \tag{36c}$$

$$\mathrm{E}\left[(\hat{\varphi}-\varphi)^2\right] \geq$$

$$\frac{1}{\frac{2\mathcal{E}_\tau}{\sigma^2}\rho^2}\left(1 + \frac{\delta_\tau^2 \Re^2\{\overline{f}_\tau\} + 2\xi_\tau \Re\{\overline{f}_\tau\}\overline{t}_\tau + \beta_\tau^2 \overline{t}_\tau^2}{\beta_\tau^2 \delta_\tau^2 - \xi_\tau^2}\right). \tag{36d}$$

The proof is given in the Appendix.

The previous equations extend classical results in [46], [51], [52] to the case where the received echo is not entirely contained in the observation window. Indeed, $\overline{t}_\tau$, $\overline{t_\tau^2}$, and δ_τ are the mean time, the mean square time, and the effective duration of the signal $s(t-\tau)$ truncated in $[0, T_r)$, respectively. As to $\overline{f}_\tau$, $\overline{f_\tau^2}$, and β_τ, they generalize the definitions of mean frequency, mean square frequency, and effective bandwidth in [46], [53] to the case where $s(t-\tau)$ is not entirely included in the observation interval; interestingly, they reduce to the definitions in [46], [53] if $T_r \geq T_s + \tau$: however, this is not the case here since T_ℓ is in general much smaller than $\tau_{\max}$.

Finally, observe that, if the baseband pulse $\psi(t)$ is real, then $\overline{ft}_\tau = 0$ and $\overline{f}_\tau$ is purely imaginary, so that $\xi_\tau = 0$. In this latter case, the bounds in (36) are inversely proportional to β_τ^2 and $\rho^2 \mathcal{E}_\tau / \sigma^2$ (the received SNR) for the range estimate, inversely proportional to δ_τ^2 and $\rho^2 \mathcal{E}_\tau / \sigma^2$ for the velocity estimate, inversely proportional to $\mathcal{E}_\tau / \sigma^2$ for the signal magnitude

estimate, and directly proportional to $1 + (\overline{t}_\tau / \delta_\tau)^2$ and inversely proportional to $\rho^2 \mathcal{E}_\tau / \sigma^2$ for the signal phase estimate.

VI. NUMERICAL ANALYSIS

The performance of the proposed detection and estimation schemes is tested here with the aid of computer simulation. We consider an IEEE 802.11ad network with a transmit power of 10 mW [54], a noise power spectral density of 2×10^{-21} W/Hz, and a noise figure of the front-end receiver of 3 dB. We model the received signal amplitude as in (12) and, unless otherwise specified, consider a Swerling I fluctuation. According to the radar equation, the term h_τ is computed as

$$h_\tau = \sqrt{\frac{G_{\text{tx}} G_{\text{rx}} \zeta}{L_\tau}} \tag{37}$$

where $G_{\text{tx}} = G_{\text{rx}} = 40$ dB are the transmit and receive antenna gains, $\zeta = 1$ m^2 is the target RCS—a typical value for a motor-cycle [55]—, and L_τ is the two-way path loss. Following [56]–[58], we modify the standard path loss in the radar equation [48], $(4\pi)^3 r^4 / \lambda^2$, as follows

$$L_\tau = \frac{(4\pi)^3}{\lambda^2} r_0^4 \left(\frac{c\tau/2}{r_0}\right)^{2\eta} \tag{38}$$

where r_0 is the close-in free space reference distance, and η is the (one-way) *best fit* path loss exponent. As in [58], we set $r_0 = 1$ m; also, following [56], [57], we choose $\eta = 2.5$ to account for the severe gases absorption effects (mainly oxygen and water vapor) at 60 GHz. In this case, Eq. (38) becomes

$$L_\tau = \frac{(4\pi)^3}{\lambda^2} \left(\frac{c\tau}{2}\right)^5. \tag{39}$$

We consider a maximum range of 190 m and a maximum speed of 15 m/s, corresponding to $\tau_{\max} = 1.27$ μs and $\nu_{\max} = 6$ kHz, and, unless otherwise stated, we set $\Delta_\tau = T$ and $\Delta_\nu = 400$ Hz, corresponding to a grid spacing of 8.52 cm in range and 1 m/s in radial velocity. The baseband pulse is a real function with support $[0, T]$, and the duration of the observation window is $T_r = 10$ μs.

The performance of the following procedures is evaluated.
a) The GLRT in (11) and the corresponding estimators in (30), labeled "GLRT-1" in the plots.
b) A simplified version of the GLRT in (11), where only a portion of the CPHY packet (the preamble, which corresponds to the first 7752 symbols) is exploited for signal detection, and the corresponding estimators in (30); this procedure is labeled "GLRT-1, simpl." in the plots.
c) The GLRT in (15), derived for the Swerling I fluctuation model, and the corresponding estimators in (30); this procedure is labeled "GLRT-2, SW-I" in the plots.
d) The GLRT in (21) and the corresponding estimator in (30a), labeled "GLRT-3" in the plots.
e) The GLRT in (22), derived for the Swerling I fluctuation model, and the corresponding estimator in (30a); this procedure is labeled "GLRT-4, SW-I" in the plots.
f) The preamble start detection and the carrier frequency offset estimation techniques used in [34], [35], [59] and

Fig. 5. Probability of false alarm versus detection threshold estimated by Monte Carlo simulation and GEVT.
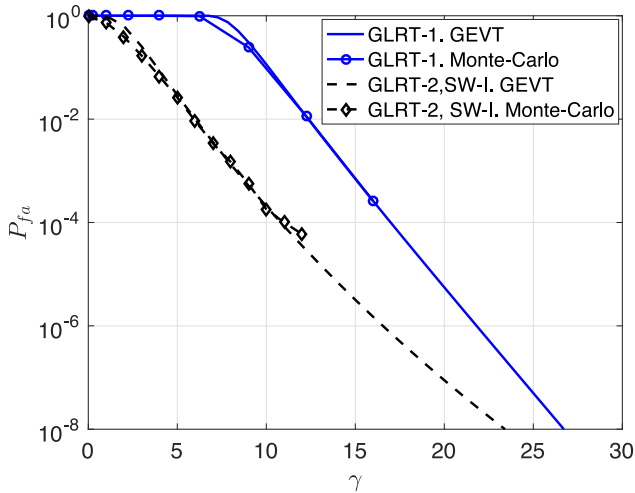

Fig. 6. Probability of false alarm versus detection threshold estimated by Monte Carlo simulation and GEVT.

included here for the sake of comparison; these techniques are labeled "Preamble-det" and "CFO-est," respectively, in the plots.

Observe that the scheme in (f) was originally devised for a different application (namely, packet synchronization); however, it can readily be adapted to our framework leveraging [34]. In particular, letting

$$R(m) = \frac{\sum_{k=0}^{127} r_0(m-k)r_0^*(m-k+128)}{\sqrt{\sum_{k=0}^{127}|r_0(m-k)|^2 \sum_{k=0}^{127}|r_0(m-k+128)|^2}}$$ (40)

$$\mathcal{C} = \left\{ m \in \mathcal{M} : \sum_{k=0}^{N_s-1} \left| R(m+k) \right| \geq \gamma \right\}$$ (41)

the detector is

$$\text{cardinality}\{\mathcal{C}\} \underset{H_0}{\overset{H_1}{\gtrless}} 0$$ (42)

and, if H_1 is declared, the range and velocity estimators are

$$\hat{r} = \frac{c}{2}\hat{m}T$$ (43a)

$$\hat{v} = \frac{\lambda}{2} \frac{\text{angle}\left\{ \sum_{k=0}^{N_s-1} R(\hat{m}+k) \right\}}{2\pi 128 T}$$ (43b)

where $\hat{m} = \min \mathcal{C}$.

In our simulation, we set a false alarm probability equal to 10^{-4}. Since, no closed-form relation is available to set the detection threshold γ, we resort to an extrapolative technique based on the generalized extreme value theory (GEVT) [60]–[62]. Figs. 5 and 6 compare the false alarm probability estimated by using the GEVT and a Monte-Carlo simulation versus γ, for Schemes (a) and (c), and for Schemes (d) and (e), respectively. Notice that the asymptotic behavior of the class-1 distribution is observed for all test statistics.

Fig. 7 shows the detection probability (P_d) as a function of the target range, $r = c\tau/2$, and the corresponding received SNR
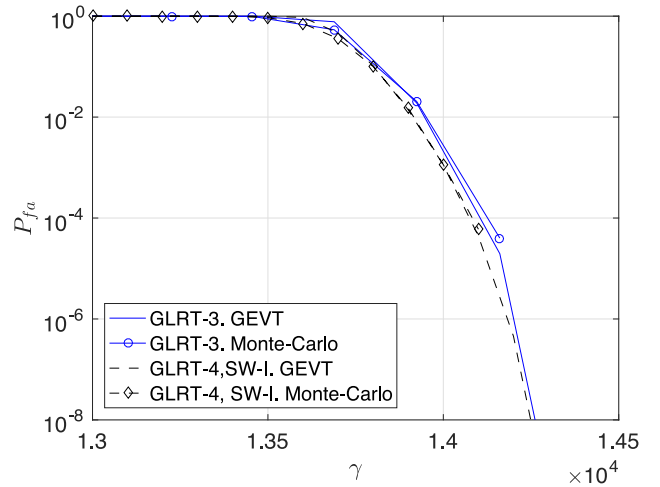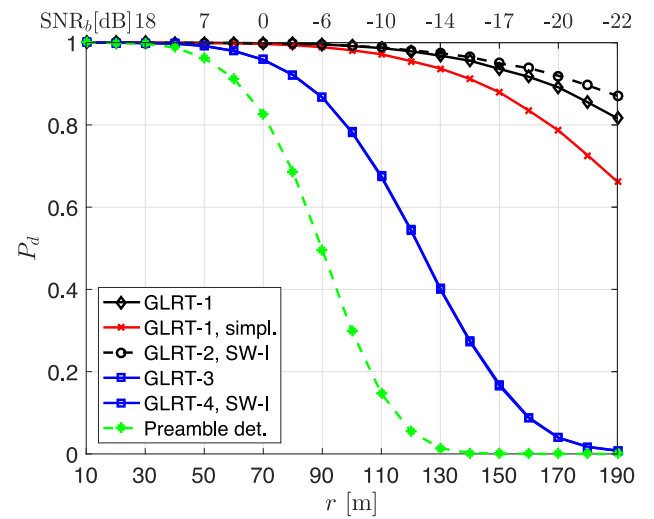

Fig. 7. Probability of detection versus range (and received SNR per symbol) for a probability of false alarm of 10^{-4}.

per symbol, defined as

$$\text{SNR}_b = \frac{h_\tau^2 \mathcal{E}_\tau}{\sigma^2 d_\tau}.$$ (44)

It is seen that all proposed detectors outperform the one in (42), especially at farther ranges (corresponding to lower values of SNR_b). The best performance is obtained by the coherent schemes, namely, (a) and (c). It should not surprise that Scheme (c) exhibits a P_d slightly higher than Scheme (a), since it exploits the prior knowledge of the distribution of the signal amplitude. Interestingly, Scheme (b) only exhibits a limited loss with respect to Scheme (a), thus suggesting that satisfactory detection/complexity tradeoffs can be achieved (notice that not only the duration of the preamble in the CPHY packet is here much shorter than T_r, but also the corresponding $\pi/2$-BPSK symbols do not change in different probed sectors). On the other hand, the incoherent Schemes (d) and (e) exhibit almost the same detection probability and, as expected, are largely outperformed by coherent counterparts.
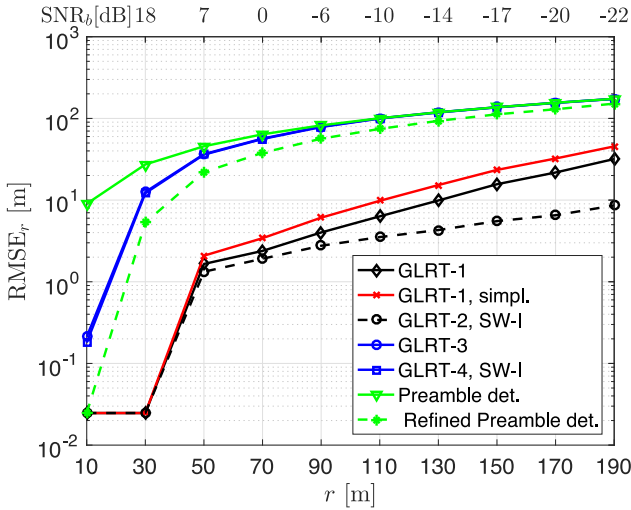
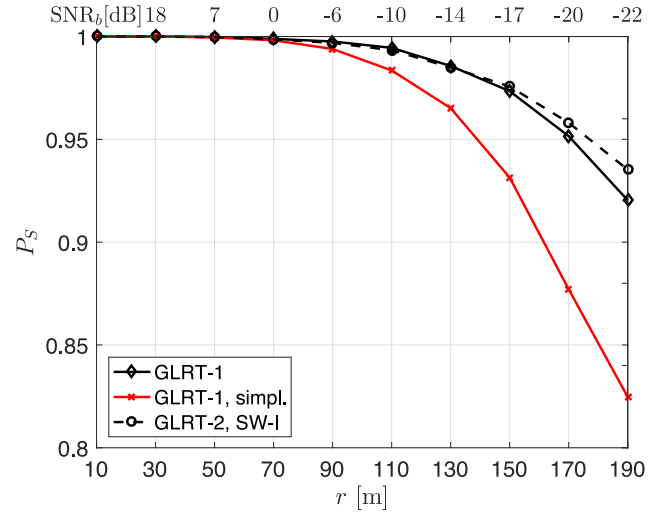Fig. 8. Root mean square error in the target range estimation versus range (and received SNR per symbol).

Fig. 9. Probability of estimating the correct target range with an accuracy smaller than the symbol interval versus range (and received SNR per symbol).

We now study the root mean square error (RMSE) in the estimation of the target range and velocity, defined as:

$$\text{RMSE}_r = \sqrt{\mathbb{E}\left[|r - \hat{r}|^2 \mid H_1\right]} \tag{45a}$$

$$\text{RMSE}_v = \sqrt{\mathbb{E}\left[|v - \hat{v}|^2 \mid H_1\right]} \tag{45b}$$

respectively. Fig. 8 reports RMSE_r versus r and SNR_b. For the sake of comparison, the performance of the *refined* estimator introduced in [34] is also included in the plot (it is labeled "Refined Preamble-det").[4] Again, the best performance is achieved by Schemes (c), (a), and (b), followed by Schemes (d) and (e), which are almost coincident, and by Scheme (f). The performance of the refined estimator in [34] is similar to that of Scheme (f) at farther ranges and to that of Schemes (a), (b), and (c) at closer ranges. Clearly, the estimation accuracy achievable by all schemes is inherently limited by the value of Δ_τ, which here is T. Schemes (a), (b), and (c) reach this limit for $r < 40\,\text{m}$, achieving a value of RMSE_r smaller than 10 cm. This accuracy is quite satisfactory for both indoor applications, such as intrusion detection in restricted environments, and outdoor applications, such as automotive radars [63]. Clearly, RMSE_r increases at farther ranges, even though it remains in the order of few meters up to a target distance of 90 m. To provide more insight on this point, we report in Fig. 9 the probability of estimating the correct target range with an accuracy smaller than the symbol interval, i.e., $P_s = \Pr\left(|\hat{r} - r| \leq cT/2\right)$, for Schemes (a), (b), and (c): it is seen that P_s remains close to one for up to 90 m. Fig. 10 shows RMSE_v versus r and SNR_b. It is seen that Schemes (a), (b), and (c) largely outperform Scheme (f), especially at farther ranges; however, their estimation accuracy is quite poor. For example, this behavior may not be satisfactory in automotive applications, where an error of at most 0.1 m/s up to 200 m is typically required [63]. On
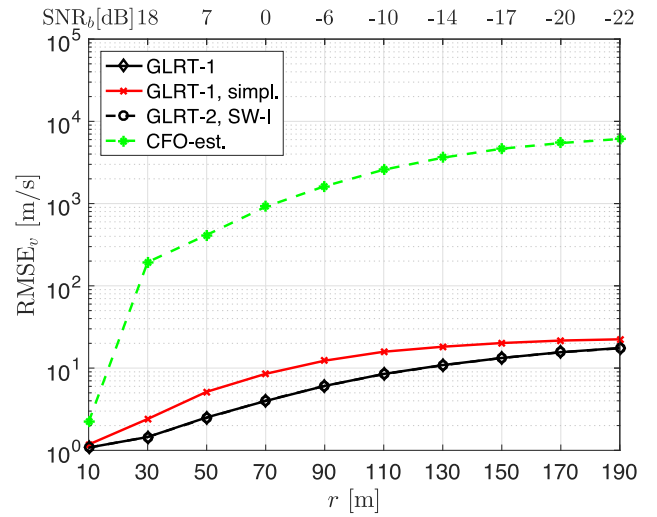

Fig. 10. Root mean square error in the target velocity estimation versus range (and received SNR per symbol).

the other hand, velocity estimation is less relevant in indoor applications.

We compare here the range and velocity estimation accuracy granted by Schemes (a) with the corresponding CRB in (36a) and (36b), respectively. Since these bounds have been obtained when the signal amplitude is an unknown deterministic parameter, we assume in our comparison $\alpha e^{i\theta} = 1$: we remark that this is different from what done in Figs. 7–10 where α is random. Fig. 11 reports RMSE_r versus r and SNR_b for three different values of Δ_τ, namely, T, $T/2$, and $T/4$. It is seen that RMSE_r is now approximately flat for all inspected ranges, meaning that the target delay is always estimated with an error at most equal to Δ_τ. Also, RMSE_r gets closer to the CRB as Δ_τ decreases; at smaller ranges, we argue that the estimation accuracy could still be improved by adopting a finer search grid in the delay domain at the price of an increased complexity. Finally, Fig. 12 reports RMSE_v versus r and SNR_b; Schemes (b) is also

---

[4]This estimator improves the range estimate in (43a) through a sliding window correlation over a narrower set of delays (384 symbols, corresponding to 3 Golay sequences).
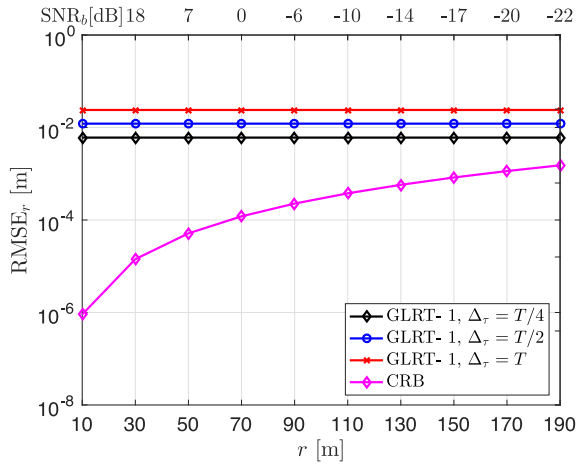
Fig. 11. Root mean square error in the target range estimation versus range (and received SNR per symbol) for different sampling intervals in the delay domain; the CRB in (36a) is also shown.
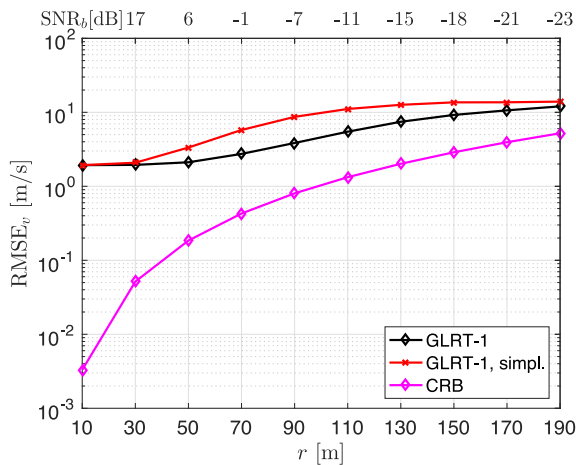

Fig. 12. Root mean square error in the target velocity estimation versus range (and received SNR per symbol); the CRB in (36b) is also shown.

included for comparison. Interestingly, the gap with respect to the CRB is quite small for $r > 70$ m; on the other hand, for $r < 70$ the achieved estimation accuracy is limited by the value of Δ_ν, which here is 400 Hz. We point out that the CRB exceeds 0.1 m/s already at $r = 30$ m, as a consequence of the very short duration of the CPHY packet; this fundamental limit confirms that the proposed opportunistic solutions are not suited for applications where an accurate estimate of the target velocity is required.

VII. Conclusions

In this work, we have studied the feasibility of an opportunistic radar which uses the IEEE 802.11ad communication standard operating at mmWaves. The control packets transmitted during the SLS phase of the beamforming protocol are exploited to opportunistically detect surrounding objects and estimate their position, radial velocity, and backscattered signal amplitude. Both coherent and incoherent detection strategies have been developed, assuming either no prior knowledge or statistical knowledge of the received signal amplitude. Interestingly, their implementation complexity can easily be tuned by adapting the

length of the observation window. The detection and estimation performance has been assessed through numerical examples, also in comparison with competing alternatives. As a benchmark, we have derived the CRB on the variance of any unbiased estimator of the unknown deterministic parameters. Our results indicate that, for a probability of false alarm of 1e-4 and Swerling-I target fluctuation, the proposed solutions can achieve close-to-one detection probability and close-to-one probability of estimating the target delay with an accuracy smaller than the symbol interval (corresponding to a range resolution smaller than 10 cm) up to 90 meters, at least for the specific channel model considered here. Also, the local accuracy on the range estimate can be improved if the delay-domain is sampled at rates larger than the symbol rate. On the other hand, the accuracy on the radial velocity estimate is limited by the very short duration of the probing signal and, generally, quite poor: for example, the CRB itself may not meet the commercial specifications enforced on the accuracy of the radial velocity estimate in some automotive applications.

While this initial study relies on some simplifying assumptions concerning the presence of at most one echo in the illumination of each sector with line-of-sight signal propagation, future studies should consider the effects of multiple received echoes due to the presence of multi-path propagation and/or the reflection from multiple objects at different range and/or azimuth: in this case, more advanced detection strategies are required to fully exploit the potentials of an opportunistic radar. Also, future studies should investigate the feasibility of a multi-frame signal processing so as to improve the radial velocity estimation and help to resolve multiple targets.

Appendix

Here we show how (36) can be obtained from (34). To this end, we first evaluate the Fisher information matrix. Recalling (4), its diagonal elements are

$$
\begin{aligned}
J_{11} &= -\mathrm{E}\left[\frac{\partial^2 \ln \Lambda_{\boldsymbol{\theta}}}{\partial \tau^2}\right] \\
&= -2\Re\left\{\frac{\rho e^{-i\varphi}}{\sigma^2}\int_0^{T_r} \mathrm{E}\left[r(t)\right]e^{-2\pi i\nu t}\frac{\partial^2 s^*(t-\tau)}{\partial \tau^2}dt\right\} \\
&\quad + \frac{\rho^2}{\sigma^2}\frac{\partial^2}{\partial \tau^2}\int_0^{T_r}\left|s(t-\tau)\right|^2 dt \\
&= \frac{2\rho^2}{\sigma^2}\left[-\Re\left\{\int_0^{T_r} s(t-\tau)\frac{\partial^2 s^*(t-\tau)}{\partial \tau^2}dt\right\}\right. \\
&\quad \left. + \frac{\partial}{\partial \tau}\Re\left\{\int_0^{T_r} s(t-\tau)\frac{\partial s^*(t-\tau)}{\partial \tau}dt\right\}\right] \\
&= \frac{2\rho^2}{\sigma^2}\int_0^{T_r}\left|\frac{\partial s(t-\tau)}{\partial \tau}\right|^2 dt \\
&= \frac{2\rho^2}{\sigma^2}\int_0^{T_r}\left|s_1(t-\tau)\right|^2 dt \\
&= \frac{2\mathcal{E}_\tau}{\sigma^2}(2\pi\rho)^2\overline{f_\tau^2} \qquad (46)
\end{aligned}
$$

$$J_{22} = -\mathrm{E}\left[\frac{\partial^2 \ln \Lambda_{\boldsymbol{\theta}}}{\partial \nu^2}\right]$$

$$= -2\Re\left\{\frac{\rho e^{-i\varphi}}{\sigma^2}\int_0^{T_r} \mathrm{E}\left[r(t)\right](-2\pi i t)^2\right.$$

$$\left.\times\, e^{-2\pi i \nu t} s^*(t-\tau)\right\}dt$$

$$= \frac{2\rho^2}{\sigma^2}\int_0^{T_r}(2\pi t)^2\left|s(t-\tau)\right|^2 dt$$

$$= \frac{2\mathcal{E}_\tau}{\sigma^2}(2\pi\rho)^2\overline{t_\tau^2} \tag{47}$$

$$J_{33} = -\mathrm{E}\left[\frac{\partial^2 \ln \Lambda_{\boldsymbol{\theta}}}{\partial \rho^2}\right]$$

$$= \frac{2}{\sigma^2}\int_0^{T_r}\left|s(t-\tau)\right|^2 dt$$

$$= \frac{2\mathcal{E}_\tau}{\sigma^2} \tag{48}$$

$$J_{44} = -\mathrm{E}\left[\frac{\partial^2 \ln \Lambda_{\boldsymbol{\theta}}}{\partial \varphi^2}\right]$$

$$= \frac{2\rho^2}{\sigma^2}\int_0^{T_r}\left|s(t-\tau)\right|^2 dt$$

$$= \frac{2\mathcal{E}_\tau}{\sigma^2}\rho^2 \tag{49}$$

while the off-diagonal ones are

$$J_{12} = -\mathrm{E}\left[\frac{\partial^2 \ln \Lambda_{\boldsymbol{\theta}}}{\partial \tau \partial \nu}\right]$$

$$= -2\Re\left\{\frac{\rho e^{-i\varphi}}{\sigma^2}\int_0^{T_r}\mathrm{E}\left[r(t)\right]\right.$$

$$\left.\times\,(-2\pi i t)e^{-2\pi i \nu t}\frac{\partial s^*(t-\tau)}{\partial \tau}dt\right\}$$

$$= 2\Re\left\{i\frac{\rho^2}{\sigma^2}\int_0^{T_r}(2\pi t)s(t-\tau)\frac{\partial s^*(t-\tau)}{\partial \tau}dt\right\}$$

$$= -2\Re\left\{i\frac{\rho^2}{\sigma^2}\int_0^{T_r}(2\pi t)s(t-\tau)s_1^*(t-\tau)dt\right\}$$

$$= \frac{2\rho^2}{\sigma^2}\Im\left\{\int_0^{T_r}(2\pi t)s(t-\tau)s_1^*(t-\tau)dt\right\}$$

$$= \frac{2\mathcal{E}_\tau}{\sigma^2}(2\pi\rho)^2\overline{ft_\tau} \tag{50}$$

$$J_{13} = -\mathrm{E}\left[\frac{\partial^2 \ln \Lambda_{\boldsymbol{\theta}}}{\partial \tau \partial \rho}\right]$$

$$= -2\Re\left\{\frac{e^{i\varphi}}{\sigma^2}\int_0^{T_r}\mathrm{E}\left[r(t)\right]e^{-2\pi i \nu t}\frac{\partial s^*(t-\tau)}{\partial \tau}dt\right\}$$

$$+ \frac{2\rho}{\sigma^2}\int_0^{T_r}\frac{\partial\left|s(t-\tau)\right|^2}{\partial \tau}dt$$

$$= -\frac{2\rho}{\sigma^2}\Re\left\{\int_0^{T_r}s(t-\tau)\frac{\partial s^*(t-\tau)}{\partial \tau}dt\right\}$$

$$+ \frac{2\rho}{\sigma^2}\int_0^{T_r}2\Re\left\{s(t-\tau)\frac{\partial s^*(t-\tau)}{\partial \tau}\right\}dt$$

$$= \frac{2\rho}{\sigma^2}\Re\left\{\int_0^{T_r}s(t-\tau)\frac{\partial s^*(t-\tau)}{\partial \tau}\right\}dt$$

$$= -\frac{2\rho}{\sigma^2}\Re\left\{\int_0^{T_r}s(t-\tau)s_1^*(t-\tau)\right\}dt$$

$$= \frac{2\mathcal{E}_\tau}{\sigma^2}2\pi\rho\Re\left\{i\overline{f_\tau}\right\}$$

$$= -\frac{2\mathcal{E}_\tau}{\sigma^2}2\pi\rho\Im\left\{\overline{f_\tau}\right\} \tag{51}$$

$$J_{14} = -\mathrm{E}\left[\frac{\partial^2 \ln \Lambda_{\boldsymbol{\theta}}}{\partial \tau \partial \varphi}\right]$$

$$= 2\Re\left\{\frac{i\rho e^{-i\varphi}}{\sigma^2}\int_0^{T_r}\mathbb{E}\left[r(t)\right]e^{-2\pi i f_d t}\frac{\partial s^*(t-\tau)}{\partial \tau}dt\right\}$$

$$= -2\Re\left\{\frac{i\rho e^{-i\varphi}}{\sigma^2}\int_0^{T_r}\mathbb{E}\left[r(t)\right]e^{-2\pi i f_d t}\frac{\partial s^*(t-\tau)}{\partial \tau}dt\right\}$$

$$= \frac{2\rho^2}{\sigma^2}\Re\left\{i\int_0^{T_r}s(t-\tau)\frac{\partial s^*(t-\tau)}{\partial \tau}dt\right\}$$

$$= -\frac{2\rho^2}{\sigma^2}\Re\left\{i\int_0^{T_r}s(t-\tau)s_1^*(t-\tau)dt\right\}$$

$$= -\frac{2\mathcal{E}_\tau}{\sigma^2}2\pi\rho^2\Re\left\{\overline{f_\tau}\right\} \tag{52}$$

$$J_{23} = -\mathrm{E}\left[\frac{\partial^2 \ln \Lambda_{\boldsymbol{\theta}}}{\partial \nu \partial \rho}\right]$$

$$= -2\Re\left\{\frac{e^{i\varphi}}{\sigma^2}\int_0^{T_r}\mathrm{E}\left[r(t)\right](-2\pi i t)e^{-2\pi i \nu t}s^*(t-\tau)dt\right\}$$

$$= 2\Re\left\{i\frac{\rho}{\sigma^2}\int_0^{T_r}(2\pi t)\left|s(t-\tau)\right|^2 dt\right\}$$

$$= 0 \tag{53}$$

$$J_{24} = -\mathrm{E}\left[\frac{\partial^2 \ln \Lambda_{\boldsymbol{\theta}}}{\partial \nu \partial \varphi}\right]$$

$$= -2\Re\left\{\frac{-i\rho e^{-i\varphi}}{\sigma^2}\int_0^{T_r}\mathbb{E}\left[r(t)\right](-2\pi i t)\right.$$

$$\left.\times\, e^{-2\pi i f_d t} s^*(t-\tau)dt\right\}$$

$$= \frac{2\rho^2}{\sigma^2}\int_0^{T_r}(2\pi t)\left|s(t-\tau)\right|^2 dt \tag{54}$$

$$= \frac{2\mathcal{E}_\tau}{\sigma^2}2\pi\rho^2\overline{t_\tau} \tag{55}$$

$$J_{34} = -\mathrm{E}\left[\frac{\partial^2 \ln \Lambda_{\boldsymbol{\theta}}}{\partial \rho \partial \phi}\right]$$

$$= -2\Re\left\{\frac{-\mathrm{i}\mathrm{e}^{-\mathrm{i}\varphi}}{\sigma^2}\int_0^{T_r}\mathrm{E}\left[r(t)\right]\mathrm{e}^{-2\pi\mathrm{i}f_d t}s^*(t-\tau)dt\right\}$$

$$= 2\Re\left\{\mathrm{i}\frac{\rho}{\sigma^2}\int_0^{T_r}\left|s(t-\tau)\right|^2 dt\right\}$$

$$= 0. \tag{56}$$

Then, we compute the inverse of the Fisher information matrix. To this end, observe that $\boldsymbol{J}$ admits the following representation

$$\boldsymbol{J} = \frac{2\mathcal{E}_\tau}{\sigma^2}\begin{pmatrix}\boldsymbol{Y} & \boldsymbol{W}\\ \boldsymbol{W}^T & \boldsymbol{Z}\end{pmatrix} \tag{57}$$

where

$$\boldsymbol{Y} = (2\pi\rho)^2\begin{pmatrix}\overline{f_\tau^2} & \overline{ft_\tau}\\ \overline{ft_\tau} & \overline{t_\tau^2}\end{pmatrix} \tag{58}$$

$$\boldsymbol{W} = -2\pi\rho\begin{pmatrix}\Im\{\overline{f}_\tau\} & \rho\Re\{\overline{f}_\tau\}\\ 0 & -\rho\overline{t}_\tau\end{pmatrix} \tag{59}$$

$$\boldsymbol{Z} = \begin{pmatrix}1 & 0\\ 0 & \rho^2\end{pmatrix}. \tag{60}$$

Therefore, from the block matrix inversion, we have

$$\boldsymbol{J}^{-1} = \frac{\sigma^2}{2\mathcal{E}_\tau}\begin{pmatrix}\boldsymbol{X} & -\boldsymbol{X}\boldsymbol{W}\boldsymbol{Z}^{-1}\\ -\boldsymbol{Z}^{-1}\boldsymbol{W}^T\boldsymbol{X} & \boldsymbol{V}\end{pmatrix} \tag{61}$$

where

$$\boldsymbol{X} = (\boldsymbol{Y} - \boldsymbol{W}\boldsymbol{Z}^{-1}\boldsymbol{W}^T)^{-1} \tag{62}$$

$$\boldsymbol{V} = \boldsymbol{Z}^{-1} + \boldsymbol{Z}^{-1}\boldsymbol{W}^T\boldsymbol{X}\boldsymbol{W}\boldsymbol{Z}^{-1}. \tag{63}$$

Since

$$\boldsymbol{X} = \left(\boldsymbol{Y} - (2\pi\rho)^2\begin{pmatrix}|\overline{f}_\tau|^2 & -\Re\{\overline{f}_\tau\}\overline{t}_\tau\\ -\Re\{\overline{f}_\tau\}\overline{t}_\tau & (\overline{t}_\tau)^2\end{pmatrix}\right)^{-1}$$

$$= \frac{1}{(2\pi\rho)^2}\begin{pmatrix}\beta_\tau^2 & \xi_\tau\\ \xi_\tau & \delta_\tau^2\end{pmatrix}^{-1}$$

$$= \frac{1}{(2\pi\rho)^2(\beta_\tau^2\delta_\tau^2 - \xi_\tau^2)}\begin{pmatrix}\delta_\tau^2 & -\xi_\tau\\ -\xi_\tau & \beta_\tau^2\end{pmatrix} \tag{64}$$

$$\boldsymbol{V} = \begin{pmatrix}1 & 0\\ 0 & \frac{1}{\rho^2}\end{pmatrix} + \frac{1}{\beta_\tau^2\delta_\tau^2 - \xi_\tau^2}\begin{pmatrix}\Im\{\overline{f}_\tau\} & 0\\ \frac{\Re\{\overline{f}_\tau\}}{\rho} & -\frac{\overline{t}_\tau}{\rho}\end{pmatrix}$$

$$\times \begin{pmatrix}\delta_\tau^2 & -\xi_\tau\\ -\xi_\tau & \beta_\tau^2\end{pmatrix}\begin{pmatrix}\Im\{\overline{f}_\tau\} & \frac{\Re\{\overline{f}_\tau\}}{\rho}\\ 0 & -\frac{\overline{t}_\tau}{\rho}\end{pmatrix}$$

$$= \begin{pmatrix}1 + \frac{\delta_\tau^2\Im^2\{\overline{f}_\tau\}}{\beta_\tau^2\delta_\tau^2 - \xi_\tau^2} & \frac{(\delta_\tau^2\Re\{\overline{f}_\tau\} + \xi_\tau\overline{t}_\tau)\Im\{\overline{f}_\tau\}}{\rho(\beta_\tau^2\delta_\tau^2 - \xi_\tau^2)}\\ \frac{(\delta_\tau^2\Re\{\overline{f}_\tau\} + \xi_\tau\overline{t}_\tau)\Im\{\overline{f}_\tau\}}{\rho(\beta_\tau^2\delta_\tau^2 - \xi_\tau^2)} & \frac{1}{\rho^2} + \frac{\delta_\tau^2\Re^2\{\overline{f}_\tau\} + 2\xi_\tau\Re\{\overline{f}_\tau\}\overline{t}_\tau + \beta_\tau^2\overline{t}_\tau^2}{\rho^2(\beta_\tau^2\delta_\tau^2 - \xi_\tau^2)}\end{pmatrix} \tag{65}$$

Eqs. (34) become

$$\mathrm{E}\left[(\hat{r} - r)^2\right] \geq \frac{\left(\frac{c}{2}\right)^2}{\frac{2\mathcal{E}_\tau}{\sigma^2}}X_{11} \tag{66a}$$

$$\mathrm{E}\left[(\hat{v} - v)^2\right] \geq \frac{\left(\frac{\lambda}{2}\right)^2}{\frac{2\mathcal{E}_\tau}{\sigma^2}}X_{22} \tag{66b}$$

$$\mathrm{E}\left[(\hat{\rho} - \rho)^2\right] \geq V_{33} \tag{66c}$$

$$\mathrm{E}\left[(\hat{\varphi} - \varphi)^2\right] \geq V_{44} \tag{66d}$$

which prove (36).

REFERENCES

[1] J. G. Andrews *et al.*, "What will 5G be?" *IEEE J. Sel. Areas Commun.*, vol. 32, no. 6, pp. 1065–1082, Jun. 2014.

[2] Y. Niu, Y. Li, D. Jin, L. Su, and A. V. Vasilakos, "A survey of millimeter wave (mmwave) communications for 5G: Opportunities and challenges," *Wireless Netw.*, vol. 21, no. 8, pp. 2657–2676, Nov. 2015.

[3] S. Buzzi, C. L. I, T. E. Klein, H. V. Poor, C. Yang, and A. Zappone, "A survey of energy-efficient techniques for 5G networks and challenges ahead," *IEEE J. Sel. Areas Commun.*, vol. 34, no. 4, pp. 697–709, Apr. 2016.

[4] Z. Pi and F. Khan, "An introduction to millimeter-wave mobile broadband systems," *IEEE Commun. Mag.*, vol. 49, no. 6, pp. 101–107, Jun. 2011.

[5] A. L. Swindlehurst, E. Ayanoglu, P. Heydari, and F. Capolino, "Millimeter-wave massive MIMO: The next wireless revolution?" *IEEE Commun. Mag.*, vol. 52, no. 9, pp. 56–62, Sep. 2014.

[6] T. S. Rappaport *et al.*, "Millimeter wave mobile communications for 5G cellular: It will work!" *IEEE Access*, vol. 1, pp. 335–349, 2013.

[7] T. S. Rappaport, R. W. Heath, Jr., J. N. Murdock, and R. C. Daniels, *Millimeter Wave Wireless Communications*. London, U.K.: Pearson, 2014.

[8] C. Gustafson, K. Haneda, S. Wyne, and F. Tufvesson, "On mm-wave multipath clustering and channel modeling," *IEEE Trans. Antennas Propag.*, vol. 62, no. 3, pp. 1445–1455, Mar. 2014.

[9] S. Hur *et al.*, "Proposal on millimeter-wave channel modeling for 5G cellular system," *IEEE J. Sel. Topics Signal Process.*, vol. 10, no. 3, pp. 454–469, Apr. 2016.

[10] M. K. Samimi and T. S. Rappaport, "3-D millimeter-wave statistical channel model for 5G wireless system design," *IEEE Trans. Microw. Theory Techn.*, vol. 64, no. 7, pp. 2207–2225, Jul. 2016.

[11] W. Roh *et al.*, "Millimeter-wave beamforming as an enabling technology for 5G cellular communications: Theoretical feasibility and prototype results," *IEEE Commun. Mag.*, vol. 52, no. 2, pp. 106–113, Feb. 2014.

[12] S. Han, C.-L. I, Z. Xu, and C. Rowell, "Large-scale antenna systems with hybrid analog and digital beamforming for millimeter wave 5G," *IEEE Commun. Mag.*, vol. 53, no. 1, pp. 186–194, Jan. 2015.

[13] M. N. Kulkarni, A. Ghosh, and J. G. Andrews, "A comparison of MIMO techniques in downlink millimeter wave cellular networks with hybrid beamforming," *IEEE Trans. Commun.*, vol. 64, no. 5, pp. 1952–1967, May 2016.

[14] S. Kutty and D. Sen, "Beamforming for millimeter wave communications: An inclusive survey," *IEEE Commun. Surveys Tuts.*, vol. 18, no. 2, pp. 949–973, Apr.–Jun. 2016.

[15] M. Bocquet *et al.*, "A multifunctional 60-GHz system for automotive applications with communication and positioning abilities based on time reversal," in *Proc. Eur. Radar Conf.*, 2010, pp. 61–64.

[16] C. Sturm and W. Wiesbeck, "Waveform design and signal processing aspects for fusion of wireless communications and radar sensing," *Proc. IEEE*, vol. 99, no. 7, pp. 1236–1259, Jul. 2011.

[17] A. R. Chiriyath, B. Paul, G. M. Jacyna, and D. W. Bliss, "Inner bounds on performance of radar and communications co-existence," *IEEE Trans. Signal Process.*, vol. 64, no. 2, pp. 464–474, Jan. 2016.

[18] H. Deng and B. Himed, "Interference mitigation processing for spectrum-sharing between radar and wireless communications systems," *IEEE Trans. Aerosp. Electron. Syst.*, vol. 49, no. 3, pp. 1911–1919, Jul. 2013.

[19] D. Ciuonzo, A. De Maio, G. Foglia, and M. Piezzo, "Intrapulse radar-embedded communications via multiobjective optimization," *IEEE Trans. Aerosp. Electron. Syst.*, vol. 51, no. 4, pp. 2960–2974, Oct. 2015.

[20] J. G. Metcale, C. Sahin, S. D. Blunt, and M. Rangaswamy, "Analysis of symbol-design strategies for intrapulse radar-embedded communications," *IEEE Trans. Aerosp. Electron. Syst.*, vol. 51, no. 4, pp. 2914–2931, Oct. 2015.

[21] A. Hassanien, M. G. Amin, Y. D. Zhang, and F. Ahmad, "Dual-function radar-communications: Information embedding using sidelobe control and waveform diversity," *IEEE Trans. Signal Process.*, vol. 64, no. 8, pp. 2168–2181, Apr. 2016.

[22] V. Winkler and J. Detlefsen, "Automotive 24 GHz pulse radar extended by a DQPSK communication channel," in *Proc. Eur. Radar Conf.*, 2007, pp. 138–141.

[23] N. Patwari and J. Wilson, "RF sensor networks for device-free localization: Measurements, models, and algorithms," *Proc. IEEE*, vol. 98, no. 11, pp. 1961–1973, Nov. 2010.

[24] J. Wilson and N. Patwari, "A fade-level skew-Laplace signal strength model for device-free localization with wireless networks," *IEEE Trans. Mobile Comput.*, vol. 11, no. 6, pp. 947–958, Jun. 2012.

[25] M. Seifeldin, A. Saeed, A. E. Kosba, A. El-Keyi, and M. Youssef, "Nuzzer: A large-scale device-free passive localization system for wireless environments," *IEEE Trans. Mobile Comput.*, vol. 12, no. 7, pp. 1321–1334, Jul. 2013.

[26] S. Savazzi, S. Sigg, M. Nicoli, V. Rampa, S. Kianoush, and U. Spagnolini, "Device-free radio vision for assisted living: Leveraging wireless channel quality information for human sensing," *IEEE Signal Process. Mag.*, vol. 33, no. 2, pp. 45–58, Mar. 2016.

[27] C. Xu, B. Firner, Y. Zhang, and R. E. Howard, "The case for efficient and robust RF-based device-free localization," *IEEE Trans. Mobile Comput.*, vol. 15, no. 9, pp. 2362–2375, Sep. 2016.

[28] *Wireless LAN Medium Access Control (MAC) and Physical Layer (PHY) Specifications. Amendment 3: Enhancements for Very High Throughput in the 60 GHz Band*, IEEE Standard 802.11ad, 2012.

[29] N. SaiShankar, D. Dash, H. El Madi, and G. Gopalakrishnan, "WiGig and IEEE 802.11ad—For multi-gigabyte-per-second WPAN and WLAN," arXiv:1211.7356, Nov. 2012.

[30] Wireless LAN at 60 GHz—IEEE 802.11ad Explained, Agilent Technologies, Santa Clara, CA, USA, May 2013.

[31] 802.11ad WILL VASTLY ENHANCE Wi-Fi the Importance of the 60 GHz Band to Wi-Fi's Continued Evolution, ABI Research, Oyster Bay, NY, USA, Apr. 2016.

[32] H. Griffiths *et al.*, "Radar spectrum engineering and management: Technical and regulatory issues," *Proc. IEEE*, vol. 103, no. 1, pp. 85–102, Jan. 2015.

[33] L. Reichardt, C. Sturm, F. Grunhaupt, and T. Zwick, "Demonstrating the use of the IEEE 802.11p car-to-car communication standard for automotive radar," in *Proc. Eur. Conf. Antennas Propag.*, 2012, pp. 1576–1580.

[34] P. Kumari, N. Gonzalez-Prelcic, and R. W. Heath, Jr., "Investigating the IEEE 802.11ad standard for millimeter wave automotive radar," in *Proc. IEEE Veh. Technol. Conf.*, 2015.

[35] W.-C. Liu, T.-C. Wei, Y.-S. Huang, C.-D. Chan, and S.-J. Jou, "All-digital synchronization for SC/OFDM mode of IEEE 802.15.3c and IEEE 802.11ad," *IEEE Trans. Circuits Syst. I, Reg. Papers*, vol. 62, no. 2, pp. 545–553, Feb. 2015.

[36] E. Grossi, M. Lops, L. Venturino, and A. Zappone, "Opportunistic automotive radar using the IEEE 802.11ad standard," in *Proc. 2017 IEEE Radar Conf.*, Seattle, WA, USA, May 2017, pp. 1196–1200.

[37] E. Grossi, M. Lops, L. Venturino, and A. Zappone, "Opportunistic radar detection in vehicular networks through the IEEE 802.11ad standard," in *Proc. 2017 IEEE 85th Veh. Technol. Conf.*, Sydney, NSW, Australia, Jun. 2017, pp. 1196–1200.

[38] T. Nitsche, C. Cordeiro, A. B. Flores, E. W. Knightly, E. Perahia, and J. C. Widmer, "IEEE 802.11ad: Directional 60 GHz communication for multi-gigabit-per-second wi-fi," *IEEE Commun. Mag.*, vol. 52, no. 12, pp. 132–141, Dec. 2014.

[39] W. Roh *et al.*, "Millimeter-wave beamforming as an enabling technology for 5G cellular communications: Theoretical feasibility and prototype results," *IEEE Commun. Mag.*, vol. 532, no. 2, pp. 1637–1652, Feb. 2014.

[40] A. Sabharwal, P. Schniter, D. Guo, D. Bliss, S. Rangarajan, and R. Wichman, "In-band full-duplex wireless: Challenges and opportunities," *IEEE J. Sel. Areas Commun.*, vol. 32, no. 9, pp. 1637–1652, Sep. 2013.

[41] N. A. Estep, D. L. Sounas, J. Soric, and A. Alu, "Magnetic-free nonreciprocity and isolation based on parametrically modulated coupled-resonator loops," *Nature Phys.*, vol. 10, no. 12, pp. 923–927, 2014.

[42] L. Li, K. Josiam, and R. Taori, "Feasibility study on full-duplex wireless millimeter-wave systems," in *Proc. Int. Conf. Acoust., Speech, Signal Process.*, May 2014, pp. 2769–2773.

[43] Z. Zhang, X. Chai, K. Long, A. V. Vasilakos, and L. Hanzo, "Full duplex techniques for 5G networks: Self-interference cancellation, protocol design, and relay selection," *IEEE Commun. Mag.*, vol. 53, no. 5, pp. 128–137, May 2015.

[44] M. Duarte *et al.*, "Design and characterization of a full-duplex multiantenna system for WiFi networks," *IEEE Trans. Veh. Technol.*, vol. 63, no. 3, pp. 1160–1177, Mar. 2014.

[45] R. T. S. Rajagopal and S. Abu-Surra, "Self-interference mitigation for inband mmwave wireless backhaul," in *Proc. IEEE 11th Consum. Commun. Netw. Conf.*, Jan. 2014, pp. 551–556.

[46] H. L. Van Trees, *Detection, Estimation, and Modulation Theory, Part III: Radar-Sonar Signal Processing and Gaussian Signals in Noise*. Hoboken, NJ, USA: Wiley, 2001.

[47] H. V. Poor, *An Introduction to Signal Detection and Estimation*. New York, NY, USA: Springer, 1994.

[48] M. I. Skolnik, *Introduction to Radar Systems*. New York, NY, USA: McGraw-Hill, 2001.

[49] E. L. Lehmann and G. Casella, *Theory of Point Estimation*, 2nd ed. New York, NY, USA: Springer, 1998.

[50] S. M. Kay, *Statistical Signal Processing: Estimation Theory*, vol. I. Englewood Cliffs, NJ, USA: Prentice-Hall, 1993.

[51] A. E. J. Kelly, "The radar measurement of range, velocity and acceleration," *IRE Trans. Mil. Electron.*, vol. MIL-5, no. 2, pp. 51–57, Apr. 1961.

[52] A. Dogandžić and A. Nehorai, "A Cramér-Rao lower bound for complex parameters," *IEEE Trans. Inf. Theory*, vol. 49, no. 6, pp. 1122–1137, Jun. 2001.

[53] D. Gabor, "Theory of communication. Part 1: The analysis of information," *J. Inst. Elect. Eng.—Part III, Radio Commun. Eng.*, vol. 93, no. 26, pp. 429–441, Nov. 1946.

[54] S. Yong, P. Xia, and A. Garcia, *60 GHz Technology for GBPS WLAN and WPAN From Theory to Practice*. Hoboken, NJ, USA: Wiley, 2011.

[55] H. Suzuki, "Measurement results of radar cross section of automobiles for millimeter wave band," in *Proc. World Congr. Intell. Syst.*, 2000.

[56] "5G channel model for bands up to 100 GHz v2.1," 2016. [Online]. Available: http://www.5gworkshops. com/5GCM.html

[57] T. S. Rappaport, E. Ben-Dor, J. N. Murdock, and Y. Qiao, "38 GHz and 60 GHz angle-dependent propagation for cellular and peer-to-peer wireless communications," in *Proc. IEEE Int. Conf. Commun.*, 2012, pp. 4568–4573.

[58] T. S. Rappaport, G. R. MacCartney, M. K. Samimi, and S. Sun, "Wideband millimeter-wave propagation measurements and channel models for future wireless communication system design," *IEEE Trans. Commun.*, vol. 63, no. 9, pp. 3029–3056, Sep. 2015.

[59] Y. S. Huang, W. C. Liu, and S. J. Jou, "Design and implementation of synchronization detection for IEEE 802.15.3c," in *Proc. Int. Symp. VLSI Des., Autom. Test*, Apr. 2011, pp. 1–4.

[60] M. Guida, D. Iovino, and M. Longo, "Comparative performance analysis of some extrapolative estimators of probability tail," *IEEE J. Sel. Areas Commun.*, vol. 6, no. 1, pp. 76–84, Jan. 1998.

[61] M. Guida, M. Longo, and M. Lops, "Logarithmic transformations for extrapolative estimation of probability tails," *Rel. Eng. Syst. Safety*, vol. 26, pp. 119–133, 1989.

[62] S. B. Weinstein, "Theory and applications of some classical and generalized asymptotic distributions of extreme values," *IEEE Trans. Inf. Theory*, vol. IT-19, no. 2, pp. 148–154, Mar. 1973.

[63] J. Hasch, E. Topak, R. Schnabel, T. Zwick, R. Weigel, and C. Wald-Schmidt, "Millimeter-wave technology for automotive radar sensors in the 77 GHz frequency band," *IEEE Trans. Microw. Theory Techn.*, vol. 60, no. 3, pp. 845–860, Mar. 2012.

Emanuele Grossi (M'08–SM'17) was born in Sora, Italy, on May 10, 1978. He received the Dr. Eng. degree in telecommunication engineering and the Ph.D. degree in electrical engineering, both from the University of Cassino and Southern Lazio, Cassino, Italy, in 2002 and 2006, respectively. In 2005, he was a Visiting Scholar with the Department of Electrical and Computer Engineering, University of British Columbia, Vancouver, BC, Canada, and in 2009, he had a visiting appointment with the Digital Technology Center, University of Minnesota, Minneapolis, MN, USA. Since February 2006, he has been an Assistant Professor with the University of Cassino and Southern Lazio. His research interests include wireless communication systems, radar detection and tracking, and statistical decision problems with emphasis on sequential analysis. Since 2017, he has been an Associate Editor for *EURASIP Signal Processing* (Elsevier).

Marco Lops (M'96–SM'01) was born in Naples, Italy. He received the Laurea and Ph.D. degrees from the University of Naples Federico II, Naples, Italy. He was an Assistant (1989–1991) and Associate (1991–2000) Professor with the University of Naples Federico II and, since March 2000, he has been a Professor with the University of Cassino and Southern Latium, Cassino, Italy. In 2009–2010, he was also a Professor with ENSEEIHT, Toulouse, France. He held visiting positions with the University of Connecticut, Rice University, University of Minnesota, Columbia University, and University of Toulouse. His research interests include detection and estimation, with emphasis on communications and radar signal processing. In 2018–2019, he was selected to serve as a Distinguished Lecturer for the Signal Processing Society. He was an Associate Editor for detection and estimation for the IEEE TRANSACTIONS ON INFORMATION THEORY, an Associate Editor for the IEEE SIGNAL PROCESSING LETTERS, and he has been an Associate Editor for the IEEE TRANSACTIONS ON SIGNAL PROCESSING since 2014.

Luca Venturino (S'03–M'06–SM'17) was born in Cassino, Italy, on August 26, 1979. He received the Ph.D. degree in electrical engineering from the University of Cassino and Southern Lazio, Cassino, Italy, in 2006. In 2004 and 2009, he was a Visiting Researcher with the Columbia University, New York, NY, USA. Between 2006 and 2008, he spent nine months with the NEC Laboratories America, Princeton, NJ, USA. He is currently an Associate Professor with the University of Cassino and Southern Lazio. His research interests include detection, estimation, and resource allocation, with emphasis on communications and radar signal processing. Since 2017, he has been an Associate Editor for the IEEE TRANSACTIONS ON SIGNAL PROCESSING and the IEEE SIGNAL PROCESSING LETTERS.

Alessio Zappone (SM'16) received the M.Sc. and Ph.D. degrees from the University of Cassino and Southern Lazio, Cassino, Italy.

He is currently a Research Associate with the LANEAS Group, Laboratoire des Signaux et Systèmes, CentraleSupélec, CNRS, Université Paris-Sud, Université Paris-Saclay, Gif-sur-Yvette, France. He was with Consorzio Nazionale Interuniversitario per le Telecomunicazioni (CNIT) in the framework of the FP7 EU-funded project TREND, which focused on energy efficiency in communication networks. From 2012 to 2016, he was the PI of the project CEMRIN on energy-efficient resource allocation in wireless networks, funded by the German Research Foundation (DFG). Since 2016, he has been an Adjoint Professor with the University of Cassino and Southern Lazio. His research interests include communication theory and signal processing, with main focus on optimization techniques for resource allocation and energy efficiency maximization. He held several research appointments at international institutions. He was the recipient of the H2020 Marie Curie IF BESMART in 2017. In 2017, he was appointed an Exemplary Reviewer for the IEEE TRANSACTIONS ON COMMUNICATIONS and the IEEE TRANSACTIONS ON WIRELESS COMMUNICATIONS. He is an Associate Editor for the IEEE SIGNAL PROCESSING LETTERS and was the Guest Editor for the IEEE JOURNAL ON SELECTED AREAS ON COMMUNICATIONS (Special Issue on Energy-Efficient Techniques for 5G Wireless Communication Systems).